SelfPowered Integrated Tactile Sensing System Based on Ultrastretchable, SelfHealing and 3D Printable Ionic Conductive Hydrogel

(Article begins on next page)

Self-Powered Integrated Tactile Sensing System Based on Ultrastretchable, Self-Healing and 3D Printable Ionic Conductive Hydrogel

Giorgio Mogli, Marco Reina, Annalisa Chiappone, Andrea Lamberti,
Candido Fabrizio Pirri, Ignazio Roppolo,* and Stefano Stassi*

Self-healing ionic conductive hydrogels have shown significant potential in applications like wearable electronics, soft robotics, and prosthetics because of their high strain sensitivity and mechanical and electrical recovery after damage. Despite the enormous interest in these materials, conventional fabrication techniques hamper their use in advanced devices since only limited geometries can be obtained, preventing proper conformability to the complexity of human or robotic bodies. Here, a photocurable hydrogel with excellent sensitivity to mechanical deformations based on a semi-interpenetrating polymeric network is reported, which holds remarkable mechanical properties (ultimate tensile strain of 550%) and spontaneous self-healing capabilities, with complete recovery of its strain sensitivity after damages. Furthermore, the developed material can be processed by digital light processing 3D printing technology to fabricate complex-shaped strain sensors, increasing mechanical stress sensitivity with respect to simple sensor geometries, reaching an exceptional pressure detection limit below 1 Pa. Additionally, the hydrogel is used as an electrolyte in the fabrication of a laser-induced graphene-based supercapacitor, then incorporated into a 3D-printed sensor to create a self-powered, fully integrated device. These findings demonstrate that by using 3D printing, it is possible to produce multifunctional, self-powered sensors, appropriately shaped depending on the various applications, without the use of bulky batteries.

G. Mogli, M. Reina, A. Lamberti, C. F. Pirri, I. Roppolo, S. Stassi
Department of Applied Science and Technology
Politecnico di Torino
C.so Duca degli Abruzzi 24, Turin 10129, Italy
E-mail: ignazio.roppolo@polito.it; stefano.stassi@polito.it
A. Chiappone
Dipartimento di Scienze Chimiche e Geologiche
Università degli studi di Cagliari
Cittadella Universitaria Blocco D, S.S. 554 bivio per Sestu, Monserrato, CA 09042, Italy
A. Lamberti, C. F. Pirri, I. Roppolo
Center for Sustainable Future Technologies @Polito
Istituto Italiano di Tecnologia
Via Livorno, 60, Turin 10144, Italy

1. Introduction

The mimicking of human haptic perception is a relevant research subject for its implication in robotics and prosthetics.[1–4] The recent rise in interest in wearable devices has focused on the development of soft sensor arrays capable of artificially reproducing human touch perception, which in Nature is provided by soft cutaneous mechanoreceptors. At the same time, soft, deformable devices have also been employed to monitor human or robotic body movements, because of their easy conformability to the complex geometry of the bodies. Bare and composite elastomeric materials are the first and most investigated solution for soft sensors, rooting their function on piezoresistive or capacitive effect.[5,6] On the other hand, this solution still shows some limitations, especially in the tuning of mechanical properties and electrical conductivity.[7,8]

Recently, hydrogel materials emerged as a suitable solution to produce ultrasensitive, highly stretchable, and transparent devices.[9–11] Hydrogels consist of a polymeric component, which constitutes the elastic solid part, dispersed in water. These materials exhibit intriguing mechanical properties such as exceptional stretchability and good mechanical recovery, which can be controlled by changing the type and the content of the polymer used. Furthermore, water provides high species mobility, making those materials ideal ionic conductors.[12] In this context, hydrogel ionic conductivity can be tuned over several orders of magnitude by properly selecting the composition and the dissolving salts in the material. Consequently, the possibility to easily tune both mechanical and electrical properties has led to their implementation in a wide range of electronic devices such as triboelectric nanogenerators,[13,14] supercapacitors,[15,16] and luminescent devices.[17,18] Furthermore, the hydrogels can mimic ionic conduction of human muscle, nervous system, and brain, thus finding applications in human and robotics wearable electronics as well as coupling artificial devices with living matter. In literature, several examples of electronic skin exploiting the stretchability, transparency, and conductivity of hydrogels have been presented with the aim of reproducing the human tactile system and

**ADVANCED
SCIENCE NEWS**

www.advancedsciencenews.com

**ADVANCED
FUNCTIONAL
MATERIALS**

www.afm-journal.de

monitoring body movements.[19–21] Indeed, the deformation of the hydrogel polymeric network induced by external tensile or compressive stress modifies the ions' diffusivity and thus ionic conductivity.[21,22] Another important characteristic of hydrogels is the possibility to include self-healing properties, exploiting the high polymeric chain mobility.[23,24] The possibility of recovering physical damages induced by stretching and deforming the sensor enhances its durability and lifetime application, further mimicking living matter. Finally, the ionic conduction in hydrogel designed for strain sensing purposes can also be harnessed to fabricate with the same material energy storage devices, such as batteries[25] and supercapacitors,[26,27] opening the way to the development of integrated self-powered hydrogel strain sensor devices. In summary, it clearly emerges that hydrogels are highly promising sensing materials for developing electronic skins.

On the other hand, despite the many examples reported in the literature, the fabrication of wearable sensors based on hydrogels is still limited to a few fabrication methods, such as casting or photolithographic process. These techniques have well-established advantages, such as the ease of implementation and the possibility to reach high spatial resolution, but own low fabrication freedom due to the need for assistive tools (masks or molds).[28] Thus, the fabrication of 3D complex structures that could guarantee improved sensing performances is hard. In this context, 3D printing technologies are a significant step forward for the development of wearable sensors with controlled geometry and properties, to mimic or to be conformable with complex natural shapes.[29,30] The exploitation of 3D printing with hydrogel materials is still growing but is mainly centered on extrusion techniques, characterized by low printing speeds, and limited spatial resolution.[31–34] Conversely, vat photopolymerization techniques, such as Digital Light Processing (DLP), which rely on sequential layer-by-layer polymerization of liquid photocurable resins through light exposure, can enable superior geometrical resolution and complexity, together with a great enhancement of printing speed.[35] Nevertheless, the most common resins commercially available for vat printing are usually based on highly reactive, lowly viscous, and low molecular weight monomers and oligomers, which generate stiff thermoset networks, which do not fulfill the request of high deformability and elasticity of the smart sensor matrices.[36] Only a few examples of the implementation of vat photopolymerization techniques for the 3D printing of hydrogel-based strain sensors are present in the literature,[37–39] indeed. Hence, it is evident that the development of vat printable stretchable, ionically conductive hydrogels, is still a challenging target.

In this work, starting on previous studies on 3D printable hydrogels,[40] a photocurable ionically conductive hydrogel based on a semi-interpenetrated network composed of poly(vinyl alcohol) (PVA), crosslinked acrylic acid-poly(ethylene glycol diacrylate) (AAc-PEGDA) and 1 M of sodium chloride (NaCl) as conductive agent (PVA/AAc/NaCl hydrogel) was developed. This possessed optimal mechanical features and self-healing ability, in addition to an elevated sensitivity and electrical response to tensile and compressive deformations. Hydrogel 3D printability through DLP technique was exploited to obtain strain sensors with complex shapes, impossible to fabricate with a standard casting approach, reaching an outstanding pressure sensitivity with a detection limit below 1 Pa. Furthermore, the same

hydrogel was employed as an electrolyte to fabricate a Laser-Induced Graphene-based supercapacitor, which was integrated into a 3D-printed sensor to achieve a completely integrated self-powered strain sensor system. In fact, along with the development of wearable sensors, the need for portable, lightweight energy storage devices has led to an increasing interest in supercapacitors due to their high power density, long lifetime, and small charge/discharging time.[41] Since hydrogels with good ionic conductivity represent an appealing solution for solid-state supercapacitor electrolytes,[42,43] they can be employed to fabricate both tactile sensors and solid-state supercapacitors to develop self-powered integrated smart systems.[44,45] The combination of these attributes demonstrates that PVA/AAc/NaCl hydrogel can serve to build multifunctional and self-powered sensors, avoiding the usage of cumbersome batteries. In addition, leveraging its 3D printability enables the production of devices tailored to specific shapes and conformability for different applications, including wearables, human-machine interfaces, and soft robotics.

2. Results and Discussion

2.1. 3D Printing and Mechanical Characterization

Based on previous research,[40] a 3D printable and self-healing poly(vinyl alcohol)-acrylic acid (PVA/AAc) hydrogel was modified to achieve piezoresistive and piezocapacitive properties. Regarding the polymeric matrix, the printability and the self-healing properties are provided by a semi-interpenetrated (semi-IPN) design of the network.[40] In fact, the synthesized material possesses both a physical network, constituted by PVA, which enables efficient self-healing thanks to the formation of entanglements and H-bonds with polar groups,[46,47] and a chemical network, based on covalent bonds formed during photoinduced copolymerization of AAc and PEGDA, which was exploited in 3D printing. Water-soluble photoinitiator nanoparticles, TPO-SDS,[48] were employed to start photopolymerization. The overall structure and manufacturing process are shown in **Figure 1**a and described in detail in Experimental Section. However, this hydrogel is little electrically conductive, and thus cannot be employed for the envisaged sensing applications. Consequently, ionic conductivity was improved by the addition of NaCl salt, dissolved in the starting water solution. This approach is easy, low cost, and already explored in literature with other hydrogel structures.[21,49–51] Nevertheless, the modification of photocurable formulations can have relevant effects, which may affect the properties and 3D printing. In this sense, the effect of the presence of salts was investigated by measuring the viscosity of the different formulations, since inks with low viscosity are preferable for the DLP technique.[52] PVA/AAc formulations with 0, 0.5, 1, 1.5, and 2 M of NaCl were tested to find the best trade-off between the printability of resin and the conductivity of the hydrogel. It was found that by increasing the NaCl concentration, the viscosity increased consequently (Figure 1b). This could be explained by the growing number of electrostatic interactions among Na^+ cations and the negatively charged COO^- groups of AAc. Moreover, the influence of NaCl on the kinetic of photopolymerization was evaluated by means of real-time photorheology to assess the printability of the inks. A fixed 1% of strain was set for remaining into the
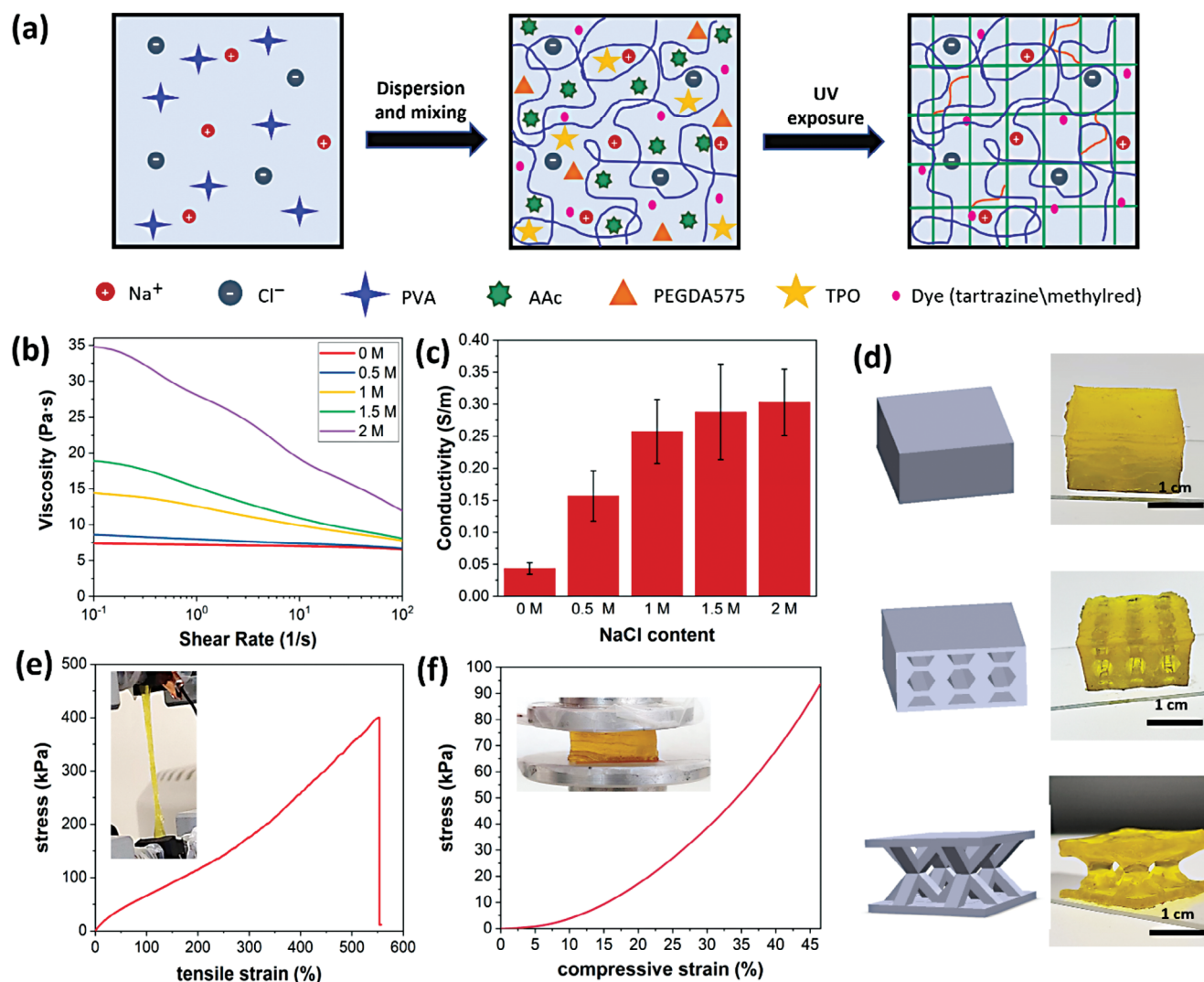
**ADVANCED
SCIENCE NEWS**

www.advancedsciencenews.com

**ADVANCED
FUNCTIONAL
MATERIALS**

www.afm-journal.de

Figure 1. 3D printable ionic conductive hydrogel. a) Scheme of composition and manufacturing process of PVA/AAc/NaCl ionically conductive hydrogel. b) Viscosities of formulations with increasing salt contents subjected to shear rate sweep. c) Conductivities of PVA/AAc/NaCl formulations with different NaCl contents. Error bars are referred to the standard deviation of 5 independent sample pools. d) Printed compression specimens (bulk, honeycomb, stars) and their STL models. e) Tensile curve of 3D-printed dumbbell sample (at a tensile test velocity of 10 mm min^{-1}). f) Compression curve of a printed parallelepiped ($2 \times 2 \times 1.5$ cm^3) at a compression velocity of 0.2 mm min^{-1}.

linear viscoelastic range (LVR) as confirmed by the stable moduli (*G'*, *G''*) in amplitude sweep tests for all the inks and cured polymers (Figure S1a,b, Supporting Information). The presence of NaCl slightly increased the reactivity of acrylate monomers as confirmed by time to reach the gel point (Figure S1e, Supporting Information). However, the storage modulus (*G'*) of all formulations reached a plateau ≈10 s after the UV source lighting (Figure S1c, Supporting Information) indicating that the polymerization process occurs at a time compatible with the DLP printing. In addition, the storage modulus, which provides a first indication of hydrogel stiffness, was higher for hydrogels with greater salt contents in the plateau area (Figure S1d, Supporting Information). This result confirmed the rheological tests.

Conductivity measurements were then carried out on hydrogel samples obtained from the five different formulations. Hydrogel specimens without salt showed low conductivity, related to the

presence of H$^+$ ions derived from carboxylic group dissociation (Figure 1c). As expected, the conductivity increased consistently by adding NaCl, thanks to the presence of more ionic species, even though this increased to reach a plateau for concentrations of NaCl over 1 M. This could be attributed to an increased concentration of cations (Na$^+$) that shields the repulsion among AAc ionized carboxylic groups (COO$^-$) linked to the molecular chains, resulting in a denser AAc network that limits ions' mobility.[53]

Consequently, since 1, 1.5, and 2 M hydrogels owned similar conductivity values, while viscosity still increased with NaCl concentration, the 1 M formulation was employed for DLP printing due to its minor viscosity.

As detailed in Experimental Section, a commercial humidifier was coupled with the printer, and water vapor flux was exploited during the printing process to avoid the evaporation of water present in the photocurable resin. This is crucial to prevent

**ADVANCED
SCIENCE NEWS**

www.advancedsciencenews.com

**ADVANCED
FUNCTIONAL
MATERIALS**

www.afm-journal.de

a rise in the viscosity of the resin during the printing process, which could compromise the entire procedure. Dyes with an absorbance superimposable to the emission light of the printer light (385 nm) were added to the formulation to improve resolution and avoid undesired curing. Printing parameters are described in detail in Experimental Section. Complex 3D models were printed (Figure 1d), exploiting the advantages of the 3D printing technology, like good repeatability, low waste material, and fidelity to virtual models. Furthermore, the DLP printing method allowed for the creation of thick structures, a challenge commonly encountered in light-induced casting manufacturing processes due to difficulties related to light penetration. At last, the best resolution achieved was ≈1 mm, which is a value in good agreement with the ones measured for similar hydrogels.[40,54] Despite this being considerably lower than the nominal resolution of the printer, different other aspects should be considered, such as kinetics of photopolymerization, mechanical characteristics of the cured material, light penetration and scattering, and viscosity of the inks, which determine final characteristics.

The printed hydrogel possessed excellent tensile properties as shown by the stretched sample in Figure 1e (inset). In fact, dumbbell-shaped specimens freshly printed were able to elongate until 550% of strain before their rupture (Figure 1e). This optimal stretchability and its soft behavior make PVA/AAc/NaCl hydrogel an ideal candidate for application in contact with irregular surfaces like those of the human body. For instance, a film of hydrogel easily matched the surface of a bent finger (Figure S2a, Supporting Information). Moreover, compressive trials on cuboid printed samples demonstrate that PVA/AAc/NaCl hydrogel could bear a 4 kg load on a small surface of 2×2 cm^2 with a compressive strain of ≈45% (Figure 1f). A compression modulus of 9.25 kPa was obtained which implies that sensors based on PVA/AAc/NaCl hydrogel could be employed as tactile sensors thanks to its mechanical properties similar to those of the human soft tissues, which own modulus between 1 and 10 kPa.[55] At last, the developed hydrogels show self-healing ability (described later), without any external trigger.[56]

2.2. Electromechanical Characterization

The presence of Na$^+$ and Cl$^-$ ions endowed hydrogel with an improved ionically conductive behavior. This was visually demonstrated by connecting an LED in series to the hydrogel. Applying a voltage to the system, the LED lights on with the hydrogel working as a conductor. Under stretching, hydrogel ionic conductivity decreases, and light becomes weaker (**Figure 2**a). This can be easily explained considering that when the hydrogel undergoes a tensile strain, the migration path of ions becomes longer. Therefore, hydrogel-based sensors' response to external strain was evaluated. Dumbbell-shaped printed sensors, with stainless steel electrodes placed at their ends, were analyzed to evaluate the printed material sensing properties. Both resistance and capacitance variations were assessed to choose the best transduction mode for tensile strain sensing. As regards piezoresistive behavior, PVA/AAc/NaCl sensors showed an increasing resistance when external strain grew. The relative variation of resistance ($\Delta R/R_0$), with respect to the resistance at no strains applied, was computed during the tensile test, and a piezoresistive

transfer curve was obtained (Figure 2b). Three separate linear regions could be highlighted. In the first one (0–100%), which involves a strain range related to human-related applications,[57] printed sensors showed a sensitivity (gauge factor) of 1.21. The gauge factor increased to 2.29 among 100% and 300% of strains and it reached the maximum value of 3.25 when the sensor was stretched between 3 and 5 times its original length. These values were comparable to other ionically conductive sensors presented in the literature.[21,39,58,59] The Piezocapacitive behavior of PVA/AAc/NaCl sensors was mainly attributable to the electric double layers formed by ions at the interface between metallic electrodes and hydrogel.[9] The capacitance transfer curve (Figure S2b, Supporting Information) exhibited a rapid quasi-linear decrease among 0% and 50% strains, approximated through a linear relationship that highlighted a sensitivity of 1.29. However, for larger tensile strains (above 200% of strain) the capacity value remains nearly constant, resulting in an almost null sensitivity. In this range, the piezocapacitive effect could be no longer used for strain sensing. For this reason, since the sensitivity in the lower strain range (under 100%) was almost similar between piezoresistive and piezocapacitive transduction modes, only the resistive behavior has been considered in the following measurements.

Cyclic electromechanical tensile measures were performed to assess the repeatability of material response. In 50 subsequent stretching–releasing trials (at 20% of strain), the amplitude of cycles of electrical resistance response was kept almost constant (Figure 2c, zoom). However, cyclic measurements revealed a small drift of the electrical response mainly due to the viscoelastic effect, which determines a dependency of the hydrogel mechanical properties on the strain deformation velocity. If the velocity of the load application is high, a residual deformation occurs, which reflects in a resistance drift.

3D printing technology was implemented to improve electrical response and conformability of sensors, by fabricating devices with complex shapes. For example, a mesh, shown in Figure 2d (inset), was designed and printed to fabricate a sensor with an enhanced tensile force sensitivity with respect to the dumbbell shape specimens exploiting both piezoresistive and piezocapacitive transduction methods. In Figure 2d the mesh relative resistance variation, in the applied tensile stress range between 0 and 30 kPa, is compared with the standard geometry response, showing a higher force sensitivity for each stress value, with an up to seven-fold sensitivity enhancement for high-stress values. Additionally, a sensitivity enhancement of about two times was observed in piezocapacitive mode (Figure S2c, Supporting Information). Therefore, mesh configuration represents a better option to build force sensing devices, since with the same applied force a mesh device would suffer a larger deformation with respect to a standard geometry device, resulting in a further increase of ion conduction path (i.e., device resistance increase).

Following the same approach, 3D-printed structures that may enhance compressive stress sensitivity were designed and printed, and their response was compared with a bulk structure. A honeycomb and a more complex structure presenting crossing beams as support elements (called here "stars") were printed (Figure 1d) to obtain larger compressive deformation with the same applied force and thus a shortening of ion conduction path with respect to bulky structure (i.e device resistance
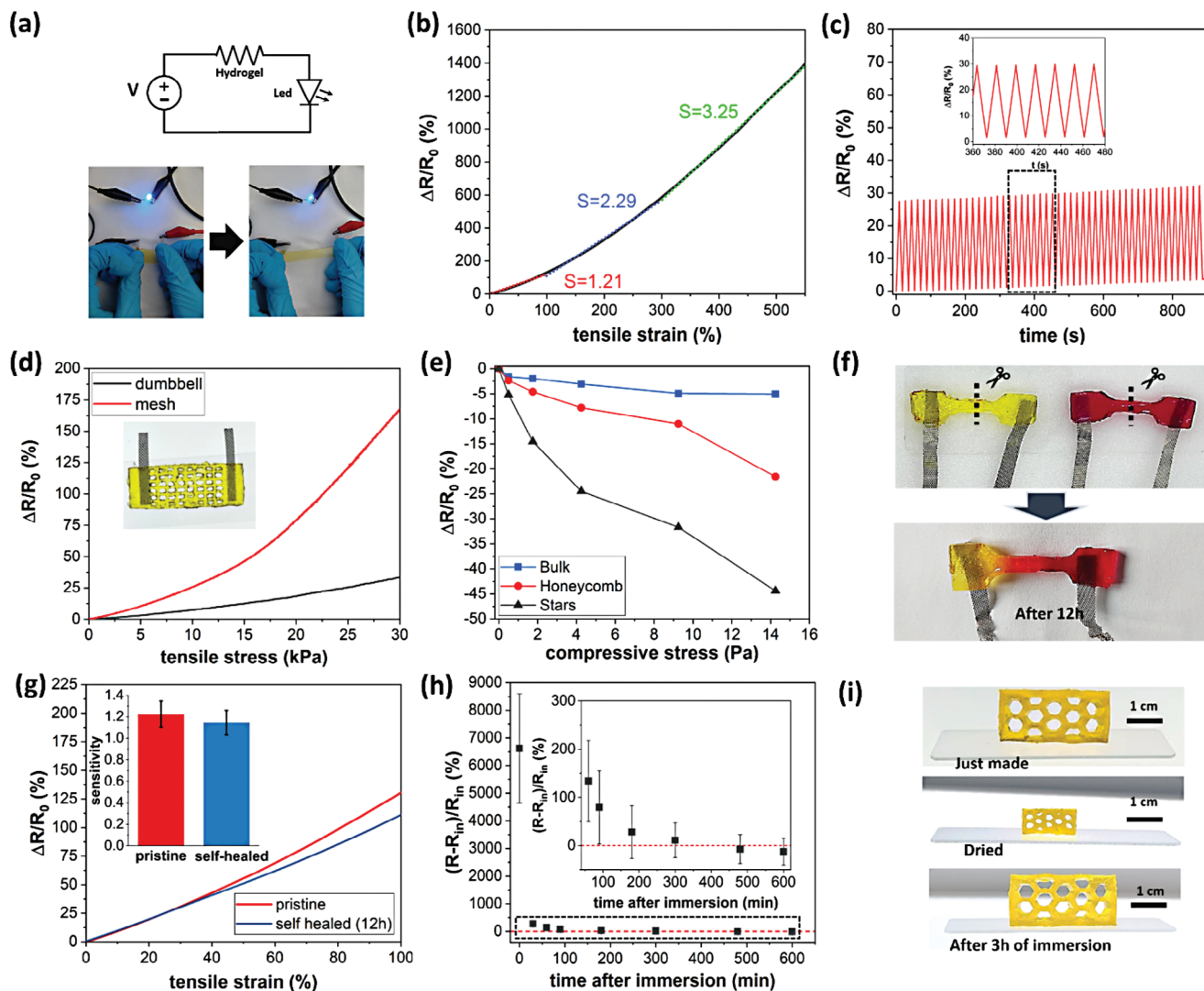
**ADVANCED
SCIENCE NEWS**

www.advancedsciencenews.com

**ADVANCED
FUNCTIONAL
MATERIALS**

www.afm-journal.de

Figure 2. Tensile and compressive stress sensitivity of self-healing 3D-printed hydrogel. a) Demonstration of electrical conductivity of PVA/AAc/NaCl hydrogel. The electrical scheme of an LED connected to the power source through a hydrogel sensor (up). Decreasing of LED light intensity when the hydrogel sensor is stretched (down). b) Electromechanical tensile tests of 3D-printed samples. Relative variation of parallel resistance versus strain of dumbbell sample. Linear fitting curves of subsequent strain regions are highlighted by different colors. c) Cyclic tensile test of a dumbbell sample stretched until 20% of strain for 50 subsequent cycles. Relative variation of resistance is reported. d) Comparison of relative resistance change versus tensile stress applied for dumbbell and mesh printed specimens. e) Relative variation of parallel resistance in compression point-by-point tests for printed samples. f) Self-healing of PVA/AAc/NaCl printed specimens: pristine samples (up) and self-healed samples after 12 h (down). g) Relative resistance variation of pristine and self-healed samples subjected to tensile test in the range 0–100% of strain. In the inset, the comparison of sensitivities (S) of pristine and 12 h self-healed samples working in piezoresistive mode. h) Recovery of electrical properties by immersion in 1 M NaCl water solution: relative variation of resistance with respect to R_{in} versus time of immersion after drying. The red line represents the initial value of resistance (0% of relative variation). Error bars refer to the standard deviation of 3 independent sample pools. i) The same 3D-printed samples were just made (up), after being stored for 30 days without controlling humidity (middle) at room temperature and after soaking in distilled water with 1 M NaCl (down).

decrease). From Figure S2c (Supporting Information), it is visible that the different geometries showed different resistance variations in response to external compressive pressures. Complex printed structures ensured an improvement in pressure sensitivity. The piezoresistive response of the three structures showed a very high sensitivity in a low-pressure working range up to 1 kPa, while above this range the sample resistance reached a saturation value and cannot sense higher pressure variation (Figure S2c, Supporting Information). Moreover, point-by-point pressure tri-

als were performed by applying small weights on the sensor to investigate the sensor's sensitivity to very low pressure (Figure 2e). All the structures showed a limit of detection below 1 Pa corresponding to an applied weight of 20 mg. In particular, the stars' geometry showed the best performance with a relative resistance variation close to 6%. This limit of detection is one of the lowest ones present in the literature[60,61] for compressive pressure sensors and is derived from the combination of the elastic mechanical properties and ion conductivity of the prepared

hydrogel. The piezocapacitive response under the compressive force of the printed hydrogel structures was also studied and showed a wider working pressure range with respect to the resistive response. Especially, the stars sample showed the highest capacitive sensitivity in the whole range of detection (Figure S2e, Supporting Information).[62–65] Its transfer curve could be approximated linearly in three different regions. Among 0–1 kPa the sensitivity of the stars sensor reaches the outstanding value of 22.11 kPa^{-1}. Then, in the range 1–9 kPa it decreases to 2.70 kPa^{-1}, but remains higher than the ones of honeycomb and bulk sensors. For higher pressures (9–12 kPa), sensitivity increases until 5.37 kPa^{-1}. Therefore, PVA/AAc/NaCl hydrogel could be printed in various shapes that enable its application as a sensor for a wide range of pressures.

2.3. Electrical Self-Healing and Recovery of PVA/AAc/NaCl Hydrogel

As mentioned above, the PVA physical network endowed PVA/AAc/NaCl sensors with self-healing properties thanks to both reversible hydrogen bonds formed and the interdiffusion ability of PVA chains.[66] This intrinsic self-healing ability was not triggered by external stimuli and therefore, proved to be an intriguing feature in simulating living tissues behavior.[67] It was visually demonstrated by cutting two printed specimens through a razor blade and, then joining their fresh-cut ends together (Figure 2f). The samples were printed using different dyes to better visualize the self-healing phenomenon. The extremities were maintained in contact for a little time, and they were immediately stuck. Self-healing was qualitatively evaluated by the diffusion of water-soluble dyes along the fracture. After 12 h the electrical behaviour of self-healed dumbbell shape specimens was analysed through point-by-point electro-tensile tests. Resistance variations of self-healed sensors result comparable to those of pristine samples as can be noticed by the curves in Figure 2g. Moreover, in the first range of tensile deformations (0–100% of strain), mainly involved in wearable applications,[68] sensitivities in piezoresistive mode remain nearly unchanged (inset Figure 2g). At a higher strain range, the piezoresistive curve of the self-healed sample is slightly different from that of the pristine sample (Figure S3a, Supporting Information) due to the difference in mechanical properties. Recovery of strain sensitivity is actually related to the restoration of mechanical properties of the material and of the conduction path that ions had to cross between the two electrodes. The tensile test (Figure S3b, Supporting Information) highlighted that the stress–strain characteristic of healed samples follows that of pristine samples in a range of strains between 0% and 200%. Elastic moduli of pristine and self-healed samples are similar indeed (Figure S3c, Supporting Information). Even though ultimate tensile strain and stress are not fully recovered (Figure S3d,e, Supporting Information), an optimal restoration of both mechanical and electrical properties under 100% of strain, namely the significant region for wearable applications, is achieved.

In view of long-term applications, the durability and possible recoverability of sensors over time are important features to assess. A batch of 3D-printed specimens was stored in open air conditions, while other samples were stored in a sealed Petri dish at 4 °C in a humid controlled environment ($R_H \approx 100\%$). After certain time steps, their electrical resistance was evaluated, and it was referred to the original resistance value computing the relative resistance variation. It can be seen from Figure S4a (Supporting Information) that the sensors stored in a controlled environment held more stable electrical properties, with a negligible resistance variation after 30 days. Otherwise, the resistance of the batch of sensors stored in open air conditions increased up to 60 times since ion mobility was lowered due to water evaporation. Indeed, the sample weight decreased by ≈50% after 1 month of storage at room temperature, indicating that almost all the water in the polymeric network (≈64%) evaporated. Conversely, samples stored in the fridge with a saturated environment maintained almost the same weight and therefore the same water content (Figure S4b, Supporting Information). Therefore, approximately after 1 month, PVA/AAc/NaCl sensors became useless since they were more rigid than pristine samples and thus no longer compliant with irregular surfaces (Figure S4c, Supporting Information). On the other hand, the sample stored at 4 °C and relative humidity (RH) ≈100% showed a similar elastic modulus with respect to the pristine sample. Moreover, the storage at controlled conditions ensured an unchanged piezoresistive behavior after 30 days while samples stored at room temperature showed a noisy response, although they are still sensitive to external strains (Figure S4d, Supporting Information). Figure 2i shows the shrinkage of the 3D-printed structure due to water loss after 1 month of storing at room temperature with no controlled humidity.

Since water evaporation results in the main problem for hydrogels, thus limiting the applicability of 3D-printed sensors here reported, the recovery of electrical properties and strain sensitivity after immersion in water were also investigated. The sensors were first completely dried, and then immersed into a 1 M NaCl water vessel. The electrical resistances of samples were measured at different time steps and the relative resistance variations with respect to the resistance of the just printed samples were computed. In Figure 2h the resistance of the original samples (represented by the dashed red line) was compared to the resistance of the same sensors immersed at different times. It can be noticed that after 3 h of immersion, the sensor resistance reached values like the original one since the average relative resistance variation was close to zero. The strain sensitivity of rehydrate samples was also tested in the 0–20% range, showing no appreciable alteration with respect to the original curve (Figure S4e, Supporting Information). Furthermore, samples have visually recovered both the original shape and dimensions after being immersed for 3 h (Figure 2i). Therefore, immersion in water with an appropriate NaCl molarity represents an easy way to restore the electrical and sensing behavior of PVA/AAc/NaCl hydrogel to achieve more durable and recyclable sensors.

2.4. Flexible Tactile Sensor

To assess the wide range of applications of PVA/AAc/NaCl sensors, printed structures were employed to measure several biometric signals, to highlight their implementation as human monitoring sensors. The hydrogel strip-shaped printed sensors were first applied to sense finger motion. In **Figure 3**a, it is shown that
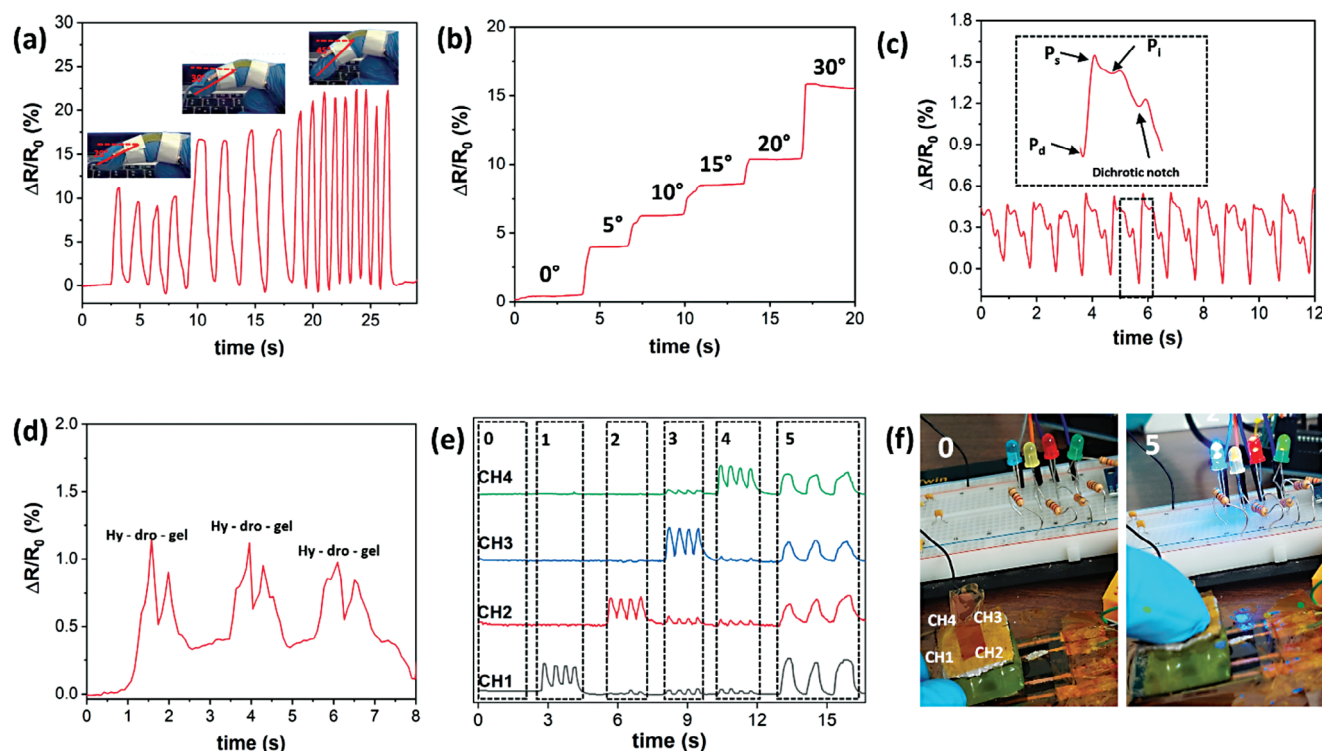
Figure 3. Hydrogel printed sensors for biometric signal analysis. Some biosignals sensed by PVA/AAc/NaCl printed sensor. a) Piezoresistive characteristic in finger bending sensing. Finger bending was performed with increasing frequencies and bending angles. b) Sensing of increasing finger bending angles. c) Heart pulse wave sensed from the wrist and its main features (P_d = diastolic pressure, P_s = systolic pressure, P_i = inflection point) d) Vocal cords vibration sensing when "hydrogel" is repeatedly pronounced. e) Stars pressure sensor used as a joypad. Normalized voltage signals when different channels are pressed individually or simultaneously. f) On the left is the experimental setup: no channels are pressed and therefore LEDs are off (corresponding to the 0 box in Figure 3e). On the right, the LEDs are turned on when all the channels are pressed simultaneously overcoming the set voltage thresholds (corresponding to box 5 in Figure 3e).

the sensor could optimally follow changes in bending frequency, showing good repeatability. Moreover, the printed device was able to sense increasing angles of bending with good stability in two subsequent steps (Figure 3b). More interestingly, the detection of subtle motions was carried out, too.

Monitoring of the pulse wave was performed by attaching the sensor to the wrist (Figure 3c). The sensor was able to recognize pulse wave shape and its characteristic points were comparable to those that can be found in literature,[69] showing the possibility of monitoring the heart-beat rate. Furthermore, subtle vibrations of the vocal cords during word pronunciation were captured by the same sensor stuck to the throat. The pattern of the resistance signals was similar when the same word (like "hydrogel") was pronounced and every syllable could be assigned to a signal peak (Figure 3d). These trials prove that biometric signals could be recorded continuously through this sensor.

Moreover, 3D printability was an interesting feature to obtain shapes that could match the requirements of specific applications, like human-machine interfaces. Here, mechanical compliance between the human sphere and the robotic one is researched. The "stars" sample (Figure 1b) was employed to build a flexible joypad made of 4 separate channels corresponding to the 4 "x-shape" columns of the structure. The sample was placed on a patterned electrode (Figure S5a, Supporting Information)

connected to the Arduino board through a multiplexer (scheme in Figure S5b, Supporting Information). Voltage data were acquired for each channel and the relative voltage variations (($V - V_0)/V_0$) with respect to their values at no pressure applied (V_0), were computed. Moreover, 4 LEDs (one per channel) were connected to the Arduino board and were switched on when an appropriate experimental threshold was overcome to have a visual demonstration. When a certain channel is pressed, a voltage increase is registered due to the reduction of the migration path that ions need to cross, and thus the local resistance decreases. Indeed, resistance and voltage are directly proportional according to the Ohm law. Figure 3e shows that when one channel is pressed, its relative voltage increases; nevertheless, it could happen that the channels near the pressed one are affected due to the propagation of deformation, but the voltage response is lower and did not cross the imposed voltage threshold as also visible from LED connected to the same channels (Figure S6, Supporting Information). When the sensor is pressed in the middle, all the channels sense the pressure in the same way and thus the voltage response is almost similar and the LEDs are switched on simultaneously (Figure 3f). Therefore, a joypad of a complex shape that can spatially discriminate pressures was built and validated. This further demonstrates that complex structures suitable for different haptic interfaces can be obtained thanks to 3D printing.
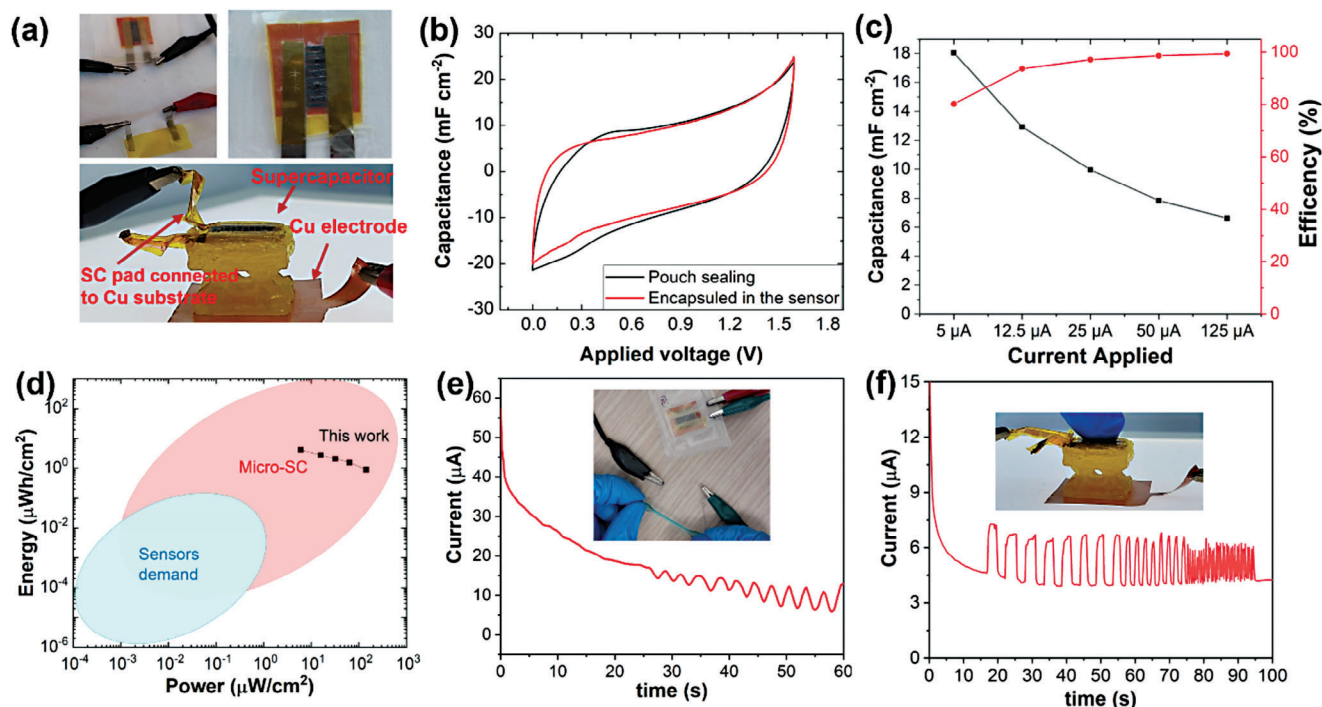
Figure 4. Hydrogel-based supercapacitor and 3D-printed self-powered sensor. a) Pictures of the integrated device with two different configurations. On top, pouch sealed supercapacitor and sensor connected with electrical terminals (left) and a zoom of sealed LIG-hydrogel supercapacitor (right). On the bottom, the supercapacitor is encapsulated on the top electrode of the sensor. b) Cyclic voltammetry was performed at 10 mV s^{-1} for the two supercapacitor configurations. c) Derived capacitance for different currents applied during CCCD. d) Ragone plot of the obtained supercapacitor, and an estimation of the sensors demand and microsupercapacitors performances[78] e) Current variation measured when the dumbbell sensor is stretched, in pouch sealing configuration. f) Current variation measured when the sensor is compressed with different velocities, in encapsulated configuration.

2.5. Self-Powered Sensor

A limitation of the sensors used for wearable and portable applications is that the electrical power needed for the sensor read-out is commonly supplied by heavy and cumbersome batteries, which limit flexible sensors' implementation in real-life tasks. Therefore, a portable supercapacitor could represent an attractive solution to overcome this issue. In this field, Laser-Induced Graphene (LIG), 3D multilayer graphene obtained by direct laser writing of polyimide (PI) substrate,[70] has been discovered as promising material due to its flexibility, low fabrication costs, and high porosity.[71] The key advantages of LIG over conventional graphene are its straightforward design, environmental friendliness, programmable compositions, and customizable morphologies[72] LIG can offer excellent electrical and thermal conductivity together with good porosity, flexibility, and mechanical toughness.[73] These LIG benefits make it possible to manufacture graphene-based energy storage devices in an intelligent way[74–76] to achieve a lightweight and portable self-powered integrated system.

By charging a supercapacitor and then connecting it in series with the hydrogel-based sensor, a self-powered portable system can be achieved. In the present case, PVA/AAc/NaCl hydrogel can be used both as sensor material and as an electrolyte for the fabrication of a supercapacitor, since it ensures good ionic conductivity. Using a LIG-interdigitated electrode prepared on a flexible polyimide substrate, a LIG-hydrogel-based supercapaci-

tor was prepared (Figure S7, Supporting Information). The supercapacitor was then connected to the hydrogel strain sensor and the current discharging on the flexible sensor was measured. When the resistance of the sensor varied due to external stimuli, the current passing through the structure changed accordingly.

Two supercapacitor sensor configurations were tested, a separate and an incorporated one. In the separated configuration (**Figure 4**a, top left) a strain flexible sensor and a LIG-hydrogel supercapacitor sealed in a pouch (Figure 4a, top right), to increase hydrogel stability, were connected via electrical terminals. In the incorporated configuration (Figure 4a, bottom) the LIG-hydrogel supercapacitor was encapsulated in a 3D-printed "stars" sensor. In this case, the supercapacitor was prepared onto a copper/polyimide bilayer substrate where the polymer layer was used for the supercapacitor electrode fabrication by graphenization, while the metal layer works as the top electrode of the sensor. The left pad of the interdigitated supercapacitor was then directly connected to the underneath copper substrate. The supercapacitor was then directly integrated on the top of the structure of the star-shaped sensor, by pouring again some hydrogel formulation and curing it with UV light to obtain a completely integrated self-powered device. The supercapacitor can be tested and charged by connecting the two LIG pads directly to the potentiostat, while the whole integrated device is tested by connecting the supercapacitor right pad and the sensor bottom electrode (electrical scheme and additional details on sensor and supercapacitor integration are present in Figure S8a,b,c, Supporting Information).

**ADVANCED
SCIENCE NEWS**

www.advancedsciencenews.com

**ADVANCED
FUNCTIONAL
MATERIALS**

www.afm-journal.de

First, the electrochemical performances of the supercapacitor prepared using the hydrogel as an electrolyte were tested. Figure 4b shows the cyclic voltammetry for both the encapsulated and sealed supercapacitors, performed at 10 mV s^{-1}. The pouch-sealed device curve seems a bit more resistive, as has also been verified by computing the equivalent series resistance (ESR) in the EIS measurement (Figure S9a, Supporting Information). The ESR for the sealed device is ≈47 Ω, while for the encapsulated supercapacitor is 28 Ω. The variation between the two ESRs is probably due only to a different adhesion of the titanium grid contact to the LIG pads. Anyway, the curves are very similar, meaning that the packaging type does not influence the performance and the hydrogel remains stable even without a sealed pouch incorporation. The potential window was then calculated by performing cyclic voltammetry with increasing potential window (Figure S9b, Supporting Information). It is possible to apply up to 1.8 V to the cell, maintaining a coulombic efficiency higher than 90%. If the voltage is further increased, current peaks due to the evolution of oxygen would strongly reduce the coulombic efficiency. This can be appreciated in Figure S9c (Supporting Information), where the efficiency decreases for voltage windows higher than 1.6 V and gets below 90% if more than 1.8 V is applied.

Figure 4c shows the capacitance and coulombic efficiency calculated when the supercapacitor is charged at 1.6 V and discharged to 0 V, applying constant currents. When a higher current is applied, the charge/discharge phases take more time as can be seen from Figure S9d (Supporting Information). Therefore, the supercapacitor will work for more time in the potential window upper limit favoring irreversible reactions that reduce the efficiency of the device. The capacitance, on the contrary, gets lower for higher currents, as expected since the device is reaching the maximum and minimum voltage in much shorter times. Therefore, the ions in the hydrogel have less time to infiltrate in the porosity of the LIG device and to form the electrical double layer. From the constant current charge/discharge (CCCD) test, power, and energy density were also computed and plotted in the Ragone plot of Figure 4d. According to Shen et al.,[77] microsupercapacitors can provide a real capacitance that satisfies the estimated energy and power requirements for many sensors (temperature, pressure, stress, etc.). The energy storage device here reported is in line with the performances analyzed in that review, thus making it suitable for integration with the smart sensor.

After electrochemical characterizations the supercapacitor has been connected to the sensor according to the configurations described above and discharge current was measured on the sensor. Results are shown in Figure 4e,f for the pouch-sealed device and the encapsulated one respectively. The discharge current follows a typical exponential decay with a time constant related to the supercapacitor capacitance value and sensor resistance. Alteration of sensor resistance due to applied strain would modify the current value up to the moment at which strain is released. Concerning the dumbbell shape sensor, when the hydrogel is stretched, the length of the path crossed by the current is increased, therefore the resistance of the load is higher, and the current decreases. Conversely, when the sensor is compressed, the reduction of resistance leads to a higher current in the circuit. From alternate stretching tests, an oscillating behavior is obtained, as shown in the curve in Figure 4e. A similar variation is shown in the encapsulated device of Figure 4f. When the device is compressed, the resistance of the sensor is reduced, and a higher current is measured, demonstrating the possibility of monitoring physical parameters with a completely integrated hydrogel-based self-powered device.

3. Conclusion

In summary, photocurable ionic conductive hydrogel based on a semi-interpenetrated polymeric network was synthesized and employed as a photocurable formulation in light-induced 3D printing. This material possessed exceptional mechanical properties (with an ultimate tensile strain of 550%) and showed the capacity for self-repair. Furthermore, it exhibited optimal sensitivity to both tensile and compressive deformations. Hydrogel 3D printability through DLP techniques was exploited to obtain strain sensors with complex shapes, impossible to fabricate with a standard casting approach, which enhances the sensor sensitivity and allows good conformability for different applications, such as wearables, human-machine interfaces, and soft robotics. Devices showing an outstanding pressure sensitivity with a detection limit below 1 Pa were demonstrated, as well as their ability to monitor biometric signals such as joint motion, heart-beat, and vocal cord vibrations. Aware of hydrogel's inherent limitations due to water evaporation, a comprehensive analysis of the sensor's lifespan in both dry and humid conditions was performed. In the case of sample drying, a method to completely restore both mechanical and sensing performance was validated.

Furthermore, the hydrogel was employed as an electrolyte to fabricate an LIG-based supercapacitor. The incorporation of the supercapacitor into a 3D-printed sensor allowed to achieve a completely integrated self-powered device, able to detect mechanical strains. These attributes confirm the potential of PVA/AAc/NaCl hydrogel-based sensors to serve as versatile, self-powered sensing devices suitable for various applications, eliminating the need for bulky batteries.

4. Experimental Section

Materials: Poly(vinyl alcohol) (M_W 89 000–98 000 Da, 99 + % hydrolyzed), acrylic acid , poly (ethylene glycol diacrylate) (average M_W 575), water-soluble diphenyl(2,4,6-trimethylbenzoyl)phospine oxide-based nanoparticle photoinitiator containing ionic surfactant (TPO-SDS), tartrazine, and methyl red sodium salt were purchased from Sigma Aldrich (USA). Commercial sodium chloride salt was employed as conductive salt. Polyimide sheets (125 µm width) were used as substrates for the supercapacitors. A titanium grid (2Ti5 – 077FA, Dexmet US) was used to contact the supercapacitor and the sensor. For the encapsulation of the supercapacitor into the sensor a bilayered foil, made by 25 µm polyimide sheet onto an 18 µm copper layer was used. Ethanol CH_3CH_2OH (Sigma Aldrich, 99.8%) and acetone CH_3COCH_3 (Sigma Aldrich, 99.5%) were employed to clean polyimide sheets and titanium grids.

3D Printable Formulation Preparation: The first step for the preparation of PVA/AAc/NaCl hydrogel precursor was dissolving sodium chloride at different concentrations (0, 0.5, 1, 1.5, and 2 м) in deionized water under magnetic stirring. Then, the solution was cooled down at 4 °C, and PVA powder was dispersed through magnetic stirring (150 rpm, 15 min), maintaining the temperature constant by immersing the container in an iced bath. Later, the temperature was gradually raised to room temperature preserving a constant stirring for 30 min. In this way, PVA powder was homogenously dispersed in a water solution. Afterward, the container was put into an oil bath at 90 °C, and the magnetic stirring rate was decreased

to 100 rpm in order to make the PVA enter into the solution. During this step, water evaporation was avoided by sealing the solution container. Approximately 1 h later, a viscous transparent solution was achieved and, after cooling to room temperature, was poured into a vial. AAc, PEGDA, TPO-SDS, and dye were added in the proper proportions and the entire solution was mixed through a centrifugal mixer (THINKY mixer AR-100) at 2000 rpm for 5 min. Tartrazine (yellow color) and methyl red (red color) were employed as dyes, to increase printing resolution and to demonstrate self-healing ability. A viscous homogeneous solution composed of 63.68% of NaCl water solution, 15.92% of PVA, 19.90% of AAc, 0.20% of PEGDA575, 0.30% of TPO-SDS, and 0.006% of dye was finally obtained. Samples for conductivity measurements were prepared by pouring resin into a rectangular mold of $15 \times 10 \times 1.5$ mm^3. Then, the resin was photocured by UV light exposition (20 mW cm^{-2}) under nitrogen flux.

Rheological Measures: Viscosities of formulations with increasing NaCl content were analyzed through rheological measurements, using an Anton Paar Physica MCR 302 rheometer in 25 mm diameter parallel plate mode. A gap of 0.2 mm between plates was set and rotation shear ramp tests between 0.01×1 and 1000×1 s^{-1} were performed.

The curing of the formulations was evaluated by real-time photorheology analysis. In this test, a 25 mm diameter parallel plate mode with a setup comprising a quartz lower plate (gap 0.2 mm) was used to measure the variation of the polymer viscoelastic properties upon light irradiation, mimicking the photopolymerization process that occurs in the VAT. The tests were performed in the linear viscoelastic region according to previous tests at a constant shear frequency of 1 Hz and a constant strain amplitude of 1% before and after polymerization. The light source used was a Hamamatsu LC8 lamp, equipped with a light guide (UV light, intensity 25 mW cm^{-2}). The light was turned on after 60 s to allow the stabilization of the system. All the rheological tests were performed at 25 °C.

3D Printing of PVA/AAc/NaCl Hydrogel Sensors: The photocurable formulation was used as ink to print 3D models employing a commercial DLP printer (Asiga MAX X UV385) with light emission wavelength centered at 385 nm and nominal resolution of 27×27 μm^2. PVA/AAc/NaCl formulation was pre-heated at 40 °C in a water bath to reduce its viscosity and to improve printability. In order to mitigate water evaporation due to the exothermic polymerization reaction, the whole printing procedure was performed under a water vapor flux (30 mL h^{-1}) generated by TaoTronics TT-AH002, similar to previous works.[40] After preliminary optimization tests, layer thickness was set at 100 μm, fixing separation velocity at 0.2 mm s^{-1} and wait time before irradiation of 3 s. To promote adhesion to the build platform, the first 4 layers were irradiated with a light intensity of 27 mW cm^{-2} for 4.5 s each, while in the following layers, light intensity was reduced to 25 mW cm^{-2} and exposure time to 3 s. After printing, the samples were cleaned employing compressed air to remove unreacted resin and then cleaned with a cloth soaked in ethanol. Sensors were produced by adding two stainless steel electrodes at the printed structure fixed by pouring a small amount of un-cured formulation and performing post-curing of 2 min in a UV oven (Robofactory UV). For specimens used in compression trials, no electrodes were added. A supercapacitor was integrated on the top surface of the pressure sensor by pouring a thin layer of formulation and irradiating it for 2 min at 20 mW cm^{-2}, to fabricate the self-powered sensor.

Electrical and Electromechanical Characterizations: Samples ionic conductivity was assessed by measuring the parallel resistance through an LCR meter (BK precision 894) using two parallel plate electrodes. A testing frequency of 1000 Hz and a voltage amplitude of 50 mV were set. Conductivity was then computed according to the formula:

$$\sigma = \frac{d}{RA} \tag{1}$$

where d is the distance between the two electrodes, R is the measured resistance and A is the surface area of the samples.

Sensors' electromechanical performances were evaluated by means of tensile and compressive tests, using a universal testing machine (Instron) while electrical impedance was measured in real-time by an LCR meter (BK precision 894). Device impedance was modeled by a parallel between a

resistance and a capacitance (R_p and C_p). For all the electrical measures a voltage amplitude of 50 mV and a testing frequency of 1000 Hz were used. As regards tensile tests, a tensile velocity of 10 mm min^{-1} was set and samples were stretched until break. Dumbbell-shaped printed samples with 30 mm length, 12 mm gauge length, 9 mm width, 3 mm gauge width, and 3 mm thickness were used. A cyclic electromechanical tensile test was also carried out by applying a tensile velocity of 20 mm min^{-1} and a maximum strain of 20% for 50 subsequent cycles. For compressive trials, a compression velocity of 0.2 mm min^{-1} was used and trials were immediately interrupted after a 5 kg load was reached. A pre-load of 5 g was set to compensate for the slight warping of the structure's top surface. Printed cuboid specimens with 20×20 mm^2 surface and 15 mm height were employed for compression tests.

Tensile point-by-point tests were performed exploiting a homemade tensile setup (from 0% to 20% with a 5% step). For each step, an electrical measurement of 1 min was performed. Compression point-by-point trials were performed by applying different weights (20, 70, 170, 370, and 870 mg) on the top surface of printed sensors (area of 20×20 mm^2). A pre-load of 5 g was used here too. As for the static tensile tests, an electrical measurement of 1 min was performed for each weight. All the tests were performed in triplicate.

Variations of relative resistance (R_p) and capacitance (C_p) were computed according to the following formulas:

$$\frac{\Delta R}{R_0} = \frac{R - R_0}{R_0} \tag{2}$$

$$\frac{\Delta C}{C_0} = \frac{C - C_0}{C_0} \tag{3}$$

Sensitivity to external deformations (S, gauge factor for piezoresistive analysis) was evaluated considering both parallel resistance (R_p) and parallel capacitance (C_p), using the formula:

$$S = \frac{\frac{\Delta X}{X_0} \, (\%)}{\epsilon \, (\%)} \tag{4}$$

where X is the electrical parameter considered (resistance or capacitance), X_0 is its value when no deformation is applied and ϵ is the strain (tensile or compressive) applied to the sample.

The self-healing mechanism was demonstrated by cutting dumbbell-shape samples with a razor blade and then putting in contact with the two ends applying a small pressure and leaving them for 12 h in a controlled humidity environment ($R_H \approx 100\%$) at 4 °C. Electrical, mechanical and sensitivity properties recovery of PVA/AAc hydrogel was assessed by subjecting 5 healed specimens to electro-mechanical tensile test (stretching up to rupture).

The durability of dumbbell-shaped samples was assessed by evaluating their resistance values at subsequent time steps, up to 30 days. A batch of specimens was maintained in a fridge (4 °C) in a sealed vessel with a controlled humidity environment. Pieces of paper soaked in water were inserted into the vessels to approximately achieve a relative humidity of 100%. Another batch was stored in a sealed container at room temperature without (25 °C) humidity control. Electro-mechanical tensile tests and weight measurements were performed on samples with different storage conditions.

Recovery trials of dried dumbbell samples were carried out by fully immersing them in 1 M NaCl water solution at different times. At each time step, resistance values were measured through an LCR meter (computing the average value of R_p on a 1 min long acquisition), and the relative variations of resistance were calculated according to the previous Formula (4).

Human signal sensing was performed by applying a printed strip of PVA/AAc/NaCl hydrogel with two stainless steel electrodes. For the joypad application, a parallel electrode configuration was used. A bottom patterned electrode (with 4 separated channels) was made of a

**ADVANCED
SCIENCE NEWS**

www.advancedsciencenews.com

**ADVANCED
FUNCTIONAL
MATERIALS**

www.afm-journal.de

copper-polyimide sheet. The upper electrode was obtained by depositing a silver coating on the surface of the hydrogel sample.

Supercapacitor Fabrication: CO_2 laser (EOX 30 W by DataLogic, Italy) was used to fabricate LIG onto 125 µm Kapton sheets. The set of employed parameters is listed in Table S1 (Supporting Information).

The variation of power, velocity, frequency of pulse, and number of dots per inch influences the dose of energy given to the sample. The reported values provide an amount of energy that allows the graphenization of the polyimide, as reported in the previous work.[74]

The microsupercapacitor was designed as a 10-finger interdigitated structure. Each digit is 4.1 mm long and 1 mm wide and the size of the whole supercapacitor is 14.4×13.5 mm^2.

Titanium grids were attached to the supercapacitor pad, then, the same formulation used to fabricate the sensors was poured and crosslinked between the interdigits, working as an electrolyte. Afterward, the device was sealed in a pouch in order to prevent the hydrogel from drying.

Finally, some of the fabricated supercapacitors were directly integrated into the structure of the star-shaped sensor, attaching the Kapton sheet to the pad of the hydrogel, then pouring again the formulation and curing it with UV light.

Electrochemical Characterizations: The electrochemical measurements were carried out using multichannel potentiostat VMP3 (Biologic, USA) in a 2-electrodes configuration. The cell was left to rest at open circuit voltage (OCP) for 10 min.

Afterward, the potentiostatic impedance spectroscopy (EIS) was performed at OCP between 10 mHz and 1 MHz. Cyclic voltammetry was carried out at 5 mV s^{-1} scan rate. Initially, 0.2 V was applied between the electrodes, then the voltage was increased progressively by 0.1 up to 2 V. Constant currents charge-discharge measurements were performed at 5, 12.5, 25, 50, and 125 µA, and the supercapacitor was charged up to 1.6 V and discharged to 0 V, in a two-electrode configuration. Biometric measurements on the human body were conducted with a volunteer under his signed consent

Conflict of Interest

The authors declare no conflict of interest.

Data Availability Statement

The data that support the findings of this study are available from the corresponding author upon reasonable request.

[1] M. Zhu, T. He, C. Lee, *Appl. Phys. Rev.* **2020**, 7, 031305.
[2] Y. J. Tan, G. J. Susanto, H. P. A. Ali, B. C. K. Tee, *Adv. Mater.* **2021**, 33, 2002800.
[3] H. Wang, M. Totaro, L. Beccai, *Adv. Sci.* **2018**, 5, 1800541.
[4] H. Yousef, M. Boukallel, K. Althoefer, *Sens. Actuators A Phys.* **2011**, 167, 171.
[5] A. Georgopoulou, F. Clemens, *ACS Appl. Electron. Mater.* **2020**, 2, 1826.
[6] C. Mu, J. Li, Y. Song, W. Huang, A. Ran, K. Deng, J. Huang, W. Xie, R. Sun, H. Zhang, *ACS Appl. Nano Mater.* **2018**, 1, 274.
[7] J. Li, L. Fang, B. Sun, X. Li, S. H. Kang, *J. Electrochem. Soc.* **2020**, 167, 037561.
[8] S. Stassi, V. Cauda, G. Canavese, C. Pirri, *Sensors* **2014**, 14, 5296.
[9] C. Yang, Z. Suo, *Nat. Rev. Mater.* **2018**, 3, 125.
[10] L. Tang, S. Wu, J. Qu, L. Gong, J. Tang, *Materials* **2020**, 13, 3947.
[11] F. Pinelli, L. Magagnin, F. Rossi, *Mater. Today Chem.* **2020**, 17, 100317.
[12] H. Yuk, B. Lu, X. Zhao, *Chem. Soc. Rev.* **2019**, 48, 1642.
[13] X. Pu, M. Liu, X. Chen, J. Sun, C. Du, Y. Zhang, J. Zhai, W. Hu, Z. L. Wang, *Sci. Adv.* **2017**, 3, e170001.
[14] W. Xu, L.-B. Huang, M.-C. Wong, L. Chen, G. Bai, J. Hao, *Adv. Energy Mater.* **2017**, 7, 1601529.
[15] X. Cao, C. Jiang, N. Sun, D. Tan, Q. Li, S. Bi, J. Song, *J. Sci.: Adv. Mater. Devices* **2021**, 6, 338.
[16] L. Jiang, X. Lu, *Mater. Chem. Front.* **2021**, 5, 7479.
[17] Q. Ma, M. Zhang, X. Xu, K.e Meng, C. Yao, Y. Zhao, J. Sun, Y. Du, D. Yang, *ACS Appl. Mater. Interfaces* **2019**, 11, 47404.
[18] B. Li, Y. Qin, Z. Li, Y. Zhang, H. Li, *Nanoscale* **2021**, 13, 11380.
[19] R. Tong, G. Chen, D. Pan, J. Tian, H. Qi, R. Li, F. Lu, M. He, *ACS Sustain. Chem. Eng.* **2019**, 7, 14256.
[20] H. Ding, Z. Xin, Z. Yang, Y. Luo, K. Xia, B. Wang, Y. Sun, J. Wang, Y. Zhang, H. Wu, S. Fan, L. Zhang, K. Liu, *Adv. Funct. Mater.* **2020**, 30, 1909616.
[21] G. Mogli, A. Chiappone, A. Sacco, C. F. Pirri, S. Stassi, *ACS Appl. Electron. Mater.* **2023**, 5, 205.
[22] B. Yang, W. Yuan, *ACS Appl. Mater. Interfaces* **2019**, 11, 16765.
[23] Y. Cao, Y. J. Tan, S. Li, W. W. Lee, H. Guo, Y. Cai, C. Wang, B. C.-K. Tee, *Nat. Electron.* **2019**, 2, 75.
[24] S. Liu, Y. Qiu, W. Yu, H. Zhang, *ACS Appl. Polym. Mater.* **2020**, 2, 1325.
[25] J. Wang, F. Tang, Y. Wang, Q. Lu, S. Liu, L. Li, *ACS Appl. Mater. Interfaces* **2020**, 12, 1558.
[26] Y. Li, Q. Gong, L. Han, X. Liu, Y. Yang, C. Chen, C. Qian, Q. Han, *Carbohydr. Polym.* **2022**, 298, 120060.
[27] J. Huang, S. Peng, J. Gu, G. Chen, J. Gao, J. Zhang, L. Hou, X. Yang, X. Jiang, L. Guan, *Mater. Horiz.* **2020**, 7, 2085.
[28] Y. Tang, B. Dai, B. Su, Y. Shi, *Front. Mater.* **2021**, 8, 658046.
[29] T. Distler, A. R. Boccaccini, *Acta Biomater.* **2020**, 101, 1.
[30] G. Ge, Q. Wang, Y. Zhang, H. N. Alshareef, X. Dong, *Adv. Funct. Mater.* **2021**, 31, 1616.
[31] S. Sun, F. Hao, X. Maimaitiyiming, *ChemistrySelect* **2022**, 7, 202203286.
[32] Z. Deng, T. Qian, F. Hang, *ACS Biomater. Sci. Eng.* **2020**, 6, 7061.
[33] J. Wei, J. Xie, P. Zhang, Z. Zou, H. Ping, W. Wang, H. Xie, J. Z. Shen, L. Lei, Z. Fu, *ACS Appl. Mater. Interfaces* **2021**, 13, 2952.
[34] Z. Zhu, H. S. Park, M. C. Mcalpine, *Sci. Adv.* **2020**, 6, 5575.
[35] G. Gonzalez, I. Roppolo, C. F. Pirri, A. Chiappone, *Addit. Manuf.* **2022**, 55, 102867.
[36] A. Salas, M. Zanatta, V. Sans, I. Roppolo, *ChemTexts* **2023**, 9, 4.
[37] Y. Rong, L. Zhu, X. Zhang, J. Fei, L. Hi, D. Huang, X. Huang, X. Yao, *Colloids Surf. A Physicochem. Eng. Asp.* **2023**, 659, 130828.
[38] Y. Wu, Y. Zeng, Y. Chen, C. Li, R. Qiu, W. Liu, *Adv. Funct. Mater.* **2021**, 31, 2107202.
[39] H. Yan, J. Zhou, C. Wang, H. Gong, W. Liu, W. Cen, G. Yuan, Y. Long, *Smart Mater. Struct.* **2022**, 31, 015019.

**ADVANCED
SCIENCE NEWS**

www.advancedsciencenews.com

**ADVANCED
FUNCTIONAL
MATERIALS**

www.afm-journal.de

[40] M. Caprioli, I. Roppolo, A. Chiappone, L. Larush, C. F. Pirri, S. Magdassi, *Nat. Commun.* **2021**, *12*, 2462.

[41] X. Sun, K. Chen, F. Liang, C. Zhi, D. Xue, *Front. Chem.* **2022**, *9*, 807500.

[42] Y. Huang, M. Zhong, Y. Huang, M. Zhu, Z. Pei, Z. Wang, Q. Xue, X. Xie, C. Zhi, *Nat. Commun.* **2015**, *6*, 10310.

[43] E. Feng, J. Li, G. Zheng, Z. Yan, X. Li, W. Gao, X. Ma, Z. Yang, *ACS Sustain. Chem. Eng.* **2021**, *9*, 7267.

[44] G. Jung, H. Lee, H. Park, J. Kim, J. W. Kim, D. S. Kim, K. Keum, Y. H. Lee, J. S. Ha, *Chem. Eng. J.* **2022**, *450*, 138379.

[45] J. Huang, S. Peng, J. Gu, G. Chen, J. Gao, J. Zhang, L. Hou, X. Yang, X. Jiang, L. Guan, *Mater. Horiz.* **2020**, *7*, 2085.

[46] J. Dahlke, S. Zechel, M. D. Hager, U. S. Schubert, *Adv. Mater. Interfaces* **2018**, *5*, 1800051.

[47] H. Zhang, H. Xia, Y. Zhao, *ACS Macro Lett.* **2012**, *1*, 1233.

[48] A. A. Pawar, G. Saada, I. Cooperstein, L. Larush, J. A. Jackman, S. R. Tabaei, N.-J. Cho, S. Magdassi, *Sci. Adv.* **2016**, *2*, e1501381.

[49] Y. Zhou, C. Wan, Y. Yang, H. Yang, S. Wang, Z. Dai, K. Ji, H. Jiang, X. Chen, Y. Long, *Adv. Funct. Mater.* **2019**, *29*, 1806220.

[50] Y. Gao, F. Jia, G. Gao, *Chem. Eng. J.* **2022**, *430*, 132919.

[51] X. Zhao, H. Wang, J. Luo, G. Ren, J. Wang, Y. Chen, P. Jia, *ACS Appl. Polym. Mater.* **2022**, *4*, 1784.

[52] J. W. Stansbury, M. J. Idacavage, *Dental Mater.* **2016**, *32*, 54.

[53] C.-J. Lee, H. Wu, Y. Hu, M. Young, H. Wang, D. Lynch, F. Xu, H. Cong, G. Cheng, *ACS Appl. Mater. Interfaces* **2018**, *10*, 5845.

[54] D. Cafiso, A. A. Septevani, C. Noè, T. Schiller, C. F. Pirri, I. Roppolo, A. Chiappone, *Sustain. Mater. Technol.* **2022**, *32*, e00444.

[55] Y. Ohm, C. Pan, M. J. Ford, X. Huang, J. Liao, C. Majidi, *Nat. Electron.* **2021**, *4*, 185.

[56] H. Zhang, H. Xia, Y. Zhao, *ACS Macro Lett.* **2012**, *1*, 1233.

[57] T. Yamada, Y. Hayamizu, Y. Yamamoto, Y. Yomogida, A. Izadi-Najafabadi, D. N. Futaba, K. Hata, *Nat. Nanotechnol.* **2011**, *6*, 296.

[58] X. Li, Y. Ma, D. Li, S. Lu, Y. Li, Z. Li, *Int. J. Biol. Macromol.* **2022**, *223*, 1530.

[59] Y. Wang, W. Zhang, X. Gong, C. Zhao, Y. Liu, C. Zhang, *ACS Biomater. Sci. Eng.* **2023**, *9*, 508.

[60] Y. X. Zhang, Y. He, Y. Liang, J. Tang, Y. Yang, H. Ming Song, M. Zrínyi, Y. M. Chen, *Appl. Surf. Sci.* **2023**, *615*, 156328.

[61] J. Zhang, Y. Hu, L. Zhang, J. Zhou, A. Lu, *Nanomicro Lett.* **2023**, *15*, 8.

[62] K. Shen, K. Xu, M. Zhang, J. Yu, Y. Yang, X. Zhao, Q. Zhang, Y. Wu, Y. Zhang, Y. Cheng, *Chem. Eng. J.* **2023**, *451*, 138525.

[63] X. Hong, H. Ding, J. Li, Y. Xue, L. Sun, F. Ding, *Polym. Adv. Technol.* **2021**, *32*, 3050.

[64] Z. Jin, H. Zhou, J. Lai, X. Jin, H. Liu, P. Wu, W. Chen, A. Ma, *ACS Appl. Polym. Mater.* **2021**, *3*, 2732.

[65] H. Zhou, J. Lai, X. Jin, H. Liu, X. Li, W. Chen, A. Ma, X. Zhou, *Chem. Eng. J.* **2021**, *413*, 127544.

[66] G. Li, H. Zhang, D. Fortin, H. Xia, Y. Zhao, *Langmuir* **2015**, *31*, 11709.

[67] T.-P. Huynh, P. Sonar, H. Haick, *Adv. Mater.* **2017**, *29*, 1604973.

[68] S. Zeng, J. Zhang, G. Zu, J. Huang, *Carbohydr. Polym.* **2021**, *267*, 118198.

[69] A. P. Avolio, M. Butlin, A. Walsh, *Physiol. Meas.* **2010**, *31*, R1.

[70] J. Lin, Z. Peng, Y. Liu, F. Ruiz-Zepeda, R. Ye, E. L. G. Samuel, M. J. Yacaman, B. I. Yakobson, J. M. Tour, *Nat. Commun.* **2014**, *5*, 5714.

[71] T.-S. D. Le, H.-P. Phan, S. Kwon, S. Park, Y. Jung, J. Min, B. J. Chun, H. Yoon, S. H. Ko, S.-W. Kim, Y.-J. Kim, *Adv. Funct. Mater.* **2022**, *32*, 2205158.

[72] P. Zaccagnini, A. Lamberti, *Appl. Phys. Lett.* **2022**, *120*, 100501.

[73] M. Parmeggiani, P. Zaccagnini, S. Stassi, M. Fontana, S. Bianco, C. Nicosia, C. F. Pirri, A. Lamberti, *ACS Appl. Mater. Interfaces* **2019**, *11*, 33221.

[74] M. Reina, A. Scalia, G. Auxilia, M. Fontana, F. Bella, S. Ferrero, A. Lamberti, *Adv. Sustain. Syst.* **2022**, *6*, 2100228.

[75] A. Lamberti, M. Serrapede, G. Ferraro, M. Fontana, F. Perrucci, S. Bianco, A. Chiolerio, S. Bocchini, *2D Mater.* **2017**, *4*, 035012.

[76] P. Zaccagnini, C. Ballin, M. Fontana, M. Parmeggiani, S. Bianco, S. Stassi, A. Pedico, S. Ferrero, A. Lamberti, *Adv. Mater. Interfaces* **2021**, *8*, 2101046.

[77] C. Shen, S. Xu, Y. Xie, M. Sanghadasa, X. Wang, L. Lin, *J. Microelectromech. Syst.* **2017**, *26*, 949.

[78] S. Choi, S. I. Han, D. Kim, T. Hyeon, D.-H. Kim, *Chem. Soc. Rev.* **2019**, *48*, 1566.